Chapter 8
Surface Improvement for Biocompatibility of Biomedical Ti Alloy by Dealloying in Metallic Melt

Masahiro Hirohashi, Kyosuke Ueda, Takeshi Wada, Takayuki Narushima, and Hidemi Kato

Abstract Dealloying is known to be a powerful method to produce porous materials mainly with noble metals because the mechanism involves the selective dissolution of specific element(s) through corrosion in acid/alkali aqueous solutions. Recently, an alternative dealloying method has been developed using a metallic melt in place of the corrosive aqueous solution. In this study, using the novel dealloying method using a metallic melt, a toxic element, Ni, was successfully removed from the surface of NiTi, which has been used for biomedical metals, for improving their biocompatibility. Although the toxic ion release per unit surface area decreased, the total amount from the treated sample did not decrease effectively because of the substantial surface area developed using the dealloying method. The dealloying method followed by the oxidation treatment was found to decrease the ion release. By optimizing the dealloying conditions to suppress surface area development, drastic improvement in the biocompatibility of these Ti alloys is expected.

Keywords Dealloying • Nitinol • Surface improvement • Biocompatibility

8.1 Introduction

Metals have often been used for biomedical applications such as operating tools and implants (fixtures, wires and stents, etc.) because of their higher strength and toughness than other types of materials and also because of additional

M. Hirohashi
Graduate Student, Graduate School of Engineering, Tohoku University, Sendai 980-8579, Japan

K. Ueda • T. Narushima
Department of Materials Processing, Tohoku University, Sendai 980-8579, Japan

T. Wada • H. Kato (✉)
Institute for Materials Research, Tohoku University, Sendai 980-8577, Japan
e-mail: hikato@imr.tohoku.ac.jp

M. Niinomi et al. (eds.), *Advances in Metallic Biomaterials*, Springer Series in Biomaterials Science and Engineering 4, DOI 10.1007/978-3-662-46842-5_8

characteristics such as superelasticity or shape memory function. Many of these applications are made of the stainless steels and Co and Ti alloys, which reluctantly contain toxic elements such as Ni, Co, V, Al, etc. to sustain the functions. Recently, many efforts have been put to develop new alloys without toxic elements. Surface improvement is an alternative method to address this problem, e.g., producing a surface barrier on NiTi to suppress Ni ion release by gas nitriding (causing TiNi and $Ti_2NiH_{0.5}$ compound layers) [1], chemical vapor deposition (CVD) (causing paracyclophane layers [2]), plasma ion implantation (causing surface layer of carbon [3] and phosphorus oxide [4]), solgel (causing TiO_2 layer [5]), and H_2O_2 (causing titania scale mainly composed of rutile and anatase [6]) methods. Although these methods can work, the resulting barrier is not sufficiently thick and is typically on the order of several hundred nm. To produce a thicker barrier, a laser spraying method has been shown to perform well [7]. However, the equipment is expensive and/or the running costs are high. Recently, our research group developed a novel dealloying method to dissolve a specific element from an alloy into a metallic melt, metallurgically, and succeeded in preparing nano-/microporous metals [8–12]. In this study, we apply this dealloying method to remove toxic elements from the surface of biomedical alloys and then investigate the resulting effect on the biocompatibility.

8.1.1 Conventional Dealloying Method

Nano-/mesoporous metals have been prepared by the dealloying (or leaching) method, which involves the selective elusion of constituent element(s) from an alloy in a corrosive aqueous solution followed by the self-organization of a porous structure by the remaining element(s). In the 1920s, for example, M. Raney succeeded in preparing porous Ni by dipping a Ni–Si alloy precursor in a sodium hydroxide aqueous solution for removal of the Si element [13]. The resulting porous product is known as the Raney Ni catalyst, which has been used for curing oils and fats. Porous metals subsequently prepared by this method have been called “Raney metals” and have been used for various kinds of catalysts. Because the mechanism of this method involves corrosion in an aqueous solution, this method can be typically applied to the preparation of porous structures with noble metals having a higher potential than the standard hydrogen electrode or for iron group elements such as Fe [14], Co [15], and Ni using the electrochemical approach. In 1979, Forty prepared porous gold by dipping a Au–Ag alloy precursor in a nitric acid aqueous solution to remove the Ag element selectively and determined that the self-organization of the porous structure was mainly achieved by surface diffusion of the remaining Au element [16]. Later, this proposed self-organization was validated by Erlebacher et al. by means of kinetic Monte Carlo simulations [17].

Although this dealloying method is simple and easy, targets are limited to the noble or iron group elements. If we attempt to apply this method to the less noble

"base" elements, the remaining elements are easily oxidized, and the process does not result in the formation of a porous structure.

8.1.2 Dealloying in a Metallic Melt

Since Raney's work, researchers have sought alternative methods to produce porous structures using base metals. To overcome this limitation, we have succeeded in using a metallic melt in place of a corrosive aqueous solution [8]. This method can also be applicable to base metals, which serve as the remaining element, because metallic melts do not ideally contain oxygen. The problem is how we design the selective dissolution of an element from an alloy precursor in a metallic melt. To understand this problem, we focus on the mixture or separation of materials. When we mix two elements, the free energy change due to this event is

$$\Delta G_{\mathrm{mix}} = \Delta H_{\mathrm{mix}} - T\Delta S_{\mathrm{mix}}, \tag{8.1}$$

where ΔH_{mix} is the heat of mixing, ΔS_{mix} is the entropy of mixing, and T is the absolute temperature. Usually, the entropy increases after mixing. Therefore, if $\Delta H_{\mathrm{mix}} < 0$, then $\Delta G_{\mathrm{mix}} < 0$, and the mixing reaction can occur spontaneously from a thermodynamic point of view. On the other hand, if $\Delta H_{\mathrm{mix}} > 0$, the sign (positive or negative) of ΔG_{mix} depends on the temperature. If the temperature is adequately controlled to make the enthalpy term larger than the entropy term, then $\Delta G_{\mathrm{mix}} > 0$, and we can avoid the mixture of the two elements. Here we dip an A–B binary alloy precursor into a metallic melt consisting of element C. If the heat of mixing between elements B and C is negative, i.e., $\Delta H_{\mathrm{mix},\,B-C} < 0$, and if the heat of mixing between elements A and C is positive, i.e., $\Delta H_{\mathrm{mix},\,A-C} > 0$, then by controlling temperature adequately only element B dissolves from the precursor into the C melt; since element A is rejected from the C melt, it is expected to self-organize into a porous structure by surface diffusion in the same manner as that of the ordinary dealloying method in an aqueous solution [16]. Figure 8.1 shows a schematic of this

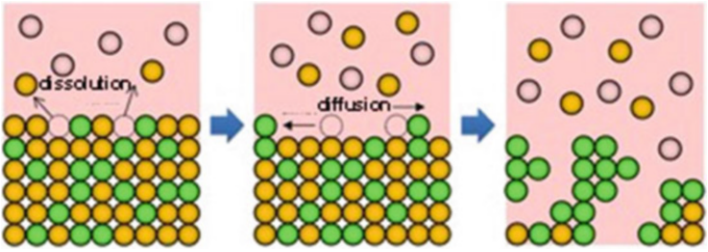

Fig. 8.1 Schematic of the dealloying method using a metallic melt, where atom B (*orange*) dissolves into a melt composed of C atoms (*pink*) and the remaining atom A (*yellowish green*) self-organizes into a porous structure by surface diffusion

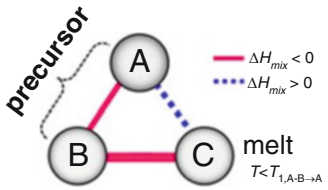

Fig. 8.2 Triangle relationship of the enthalpies of mixing among elements A, B, and C for dealloying in a metallic melt

novel dealloying method that involves the selective dissolution of B atoms (orange) in the C atom melt (pink) and surface diffusion of the remaining A atoms (yellowish green). Figure 8.2 summarizes this "triangle" relationship in terms of the heat of mixing among elements A, B, and C required for the dealloying reaction in a metallic melt. Because the heat of mixing is expressed usually with temperature and chemical composition, we have to calculate the rigid value with considering these parameters for the heat of mixing with these parameters for designing the dealloying reaction. However, this is sometimes complicated. The heat of mixing between the transition metals and the transition metals and metalloids can be obtained from the table in Ref. [18], the values of which are approximately calculated by the Miedema model and that of other metals can be obtained from the table constructed by Takeuchi et al. [19]. In our study, we first identify the candidates for elements A, B, and C from these values, and we then confirm the relationships A–B and B–C (mixture) and A–C (separation) by the related binary phase diagrams. The following are demonstrations of the design of the dealloying reaction in a metallic melt for preparing porous hcp-Ti (α-Ti) and bcc-Ti (β-Ti) alloys as examples.

8.2 Porous α-Ti and β-Ti Alloy Prepared by Dealloying with a Metallic Melt

8.2.1 α-Ti [8]

The values of heat of mixing between various elements are tabulated in Table 8.1, which include some RE (rare earth) metal candidates. Here, A = Ti and candidates for the other suitable elements appropriate to the triangle relationship described by Fig. 8.2 are selected from the table to be B = Cu and C = Mg. As shown in Fig. 8.3a, the Ti–Cu binary system includes a solid solution and intermetallic compounds; thus, this binary system can be used for the precursor. It is confirmed from the related phase diagrams [20] shown in Fig. 8.3b, c that Mg alloys with Cu (Fig. 8.3b), which is expected to dissolve from the precursor, while on the other hand, Mg separates from the Ti element over wide composition and temperature ranges (Fig. 8.3c). The nominal composition of the precursor is determined to be $Ti_{30}Cu_{70}$ at%. The ingot is prepared by arc-melting high-purity Ti (99.99 mass%) and Cu (99.99 mass%) metals in an argon atmosphere. Thin ribbons of the Ti–Cu

Table 8.1 Enthalpies of mixing (kJ/mol) among A = Ti, B = Ni, and C = Mg, Ca, and Ce (rare earth), where A, B, and C satisfy the triangle relationship shown in Fig. 8.2

	A	B	C			
	Ti	Cu	Ni	Mg	Ca	Ce
Ti		−9	−35	+16	+43	+18
Cu				−3	−13	−21
Ni				−4	−7	−28

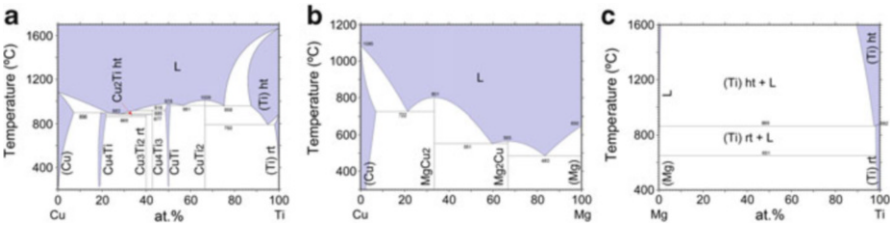

Fig. 8.3 Binary phase diagrams for Ti–Cu (**a**), Cu–Mg (**b**), and Mg–Ti (**c**)

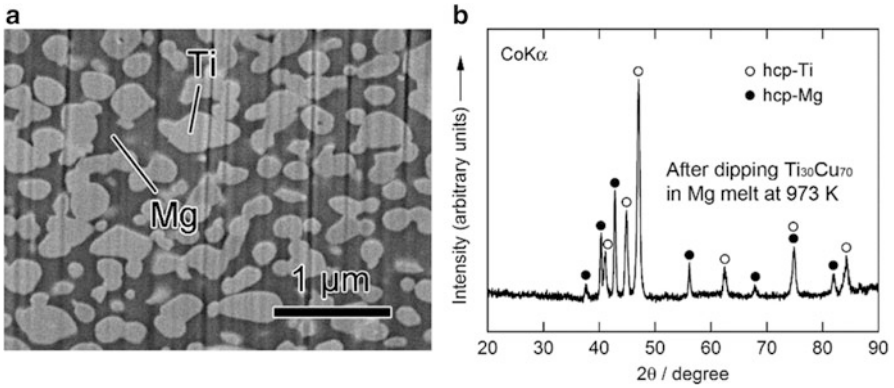

Fig. 8.4 Scanning electron microscope (SEM) image of a polished surface of $Ti_{30}Cu_{70}$ (at%) alloy dipped in a Mg melt at 973 K for 5 s (**a**) and a corresponding XRD pattern from the surface (**b**) (Reprinted from Ref. [8], Copyright 2011, with permission from Elsevier)

alloy about 10 mm wide and 30 μm thick were prepared by the melt-spinning method. The x-ray diffraction (XRD) pattern of the ribbon is a broad halo pattern (not shown), which is a characteristic of an amorphous structure; however, it has been confirmed that the dealloying reaction does not depend so much on the precursor structure, and crystalline alloy structures are also acceptable. About 10 g of Mg (99.9 mass%) was inductively heated in a carbon crucible under an argon atmosphere to create a pure liquid. The Mg melt must be maintained at a temperature less than 1,233 K, which is the lowest liquid temperature of the $Ti_{57}Cu_{43}$ (at%) alloy (see Fig. 8.3a), to avoid mixing the Ti–Cu alloy system with a titanium concentration from 30 at% to 100 at% together with the melt in a liquid state. Here, we set the melt temperature at 973 K and the dipping time to 5 s. Figure 8.4 shows (a) a scanning electron microscopy (SEM) image of a polished

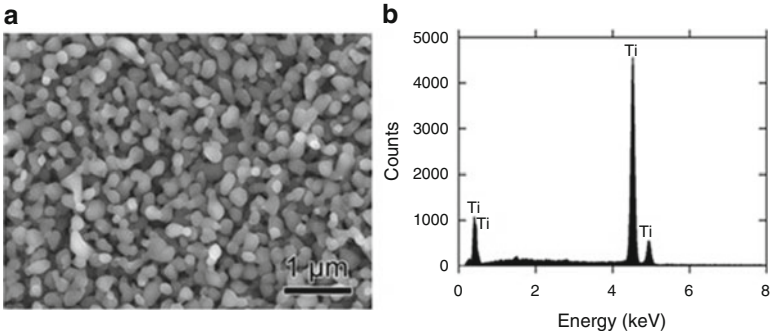

Fig. 8.5 SEM image of the bending fracture surface of porous Ti prepared by dipping the $Ti_{30}Cu_{70}$ (at%) alloy into a Mg melt followed by leaching the Mg phases in a nitric acid aqueous solution (**a**) and the EDX result obtained from the central part of the fracture surface (**b**) (Reprinted from Ref. [8], Copyright 2011, with permission from Elsevier)

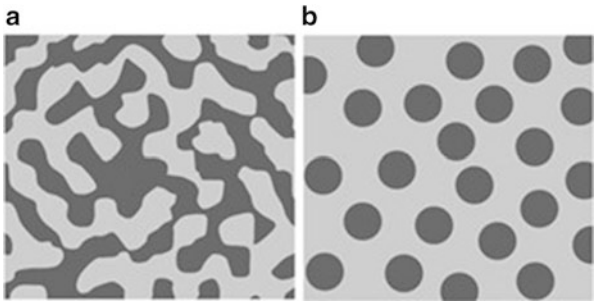

Fig. 8.6 Schematic of typical composite structures: bicontinuous (**a**) and isolated (**b**)

cross section of the ribbon precursor dipped in the Mg melt and (b) the XRD pattern of the bulk precursor dipped in the Mg melt under nearly the same conditions as the ribbon precursor shown in (a). It is recognized that the $Ti_{30}Cu_{70}$ alloy precursor became a nanocomposite consisted of hcp-Ti regions of about 200 nm in size surrounded by hcp-Mg regions after dipping in the Mg melt, which can be confirmed by the XRD pattern shown in Fig. 8.4b. The nanocomposite was dipped in a nitric acid aqueous solution to remove the Mg phase, and then the bending fracture surface was evaluated by SEM-energy dispersive x-ray spectroscopy (SEM-EDX). The results in Fig. 8.5 show that the nanocomposite became a porous structure of pure Ti consisting of hcp-Ti particles of ~200 nm size partially bonded together, and no Mg phase was detected even around the central part of the fracture surface. Evidently, the nitric acid aqueous solution penetrated from the surface of the sample and dissolved all traces of Mg phase inside the material. In other words, the original Ti/Mg nanocomposite was a completely bicontinuous structure, as schematically shown in Fig. 8.6a, in comparison with the isolated structure shown in Fig. 8.6b, and all pores remaining after the removal of Mg are connected

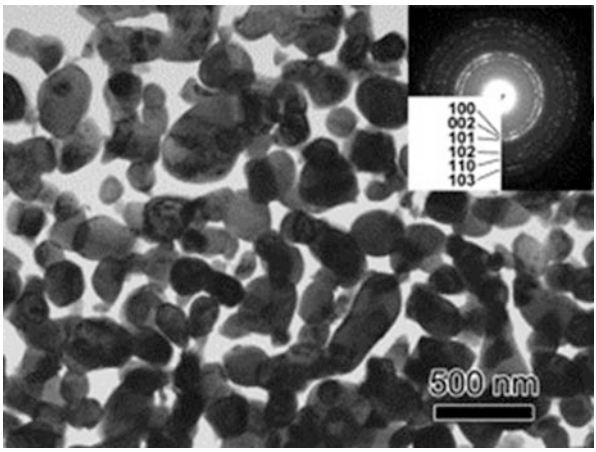

Fig. 8.7 Transmission electron microscope (TEM) image of porous Ti with its corresponding electron diffraction pattern in the inset (Reprinted from Ref. [8], Copyright 2011, with permission from Elsevier)

to the outside of the sample. Figure 8.7 shows a transmission electron microscopy (TEM) image and a selected area electron diffraction pattern of the nanoporous Ti. The presence of Ti particles of a diameter of about 200 nm without grain boundaries indicates that the particles are single crystals. Thus, the porous structure was formed by partially connected Ti single crystals. Based on the same reaction design, open-cell-type nanoporous metals were formed from base metals such as Fe, Cr [10], Nb [11], and even a metalloid of Si [21], confirming the universality of this reaction design of dealloying in a metallic melt. Figure 8.8 shows SEM images of the fracture surfaces of these various nanoporous base metals, and the insets demonstrate the triangle relationships used in the preparation of each nanoporous metal.

Here, we summarize the preparation procedures for nanoporous metals and nanocomposites by dealloying in a metallic melt, as they are schematically shown in Fig. 8.9:

1. Selection of A–B–C elements, which satisfy the triangle relationship of the heats of mixing (tables of values of heat of mixing and equilibrium phase diagrams can be used)
2. Preparation of the A–B alloy precursor
3. Selective dissolution of element B from the A–B precursor into the C metal melt (formation of the porous structure)
4. Removal of the C element by etching with an acid or alkaline solution (the remaining A component must be inert in the solution)

For preparing nanocomposites, the 4th step of the process is not required.

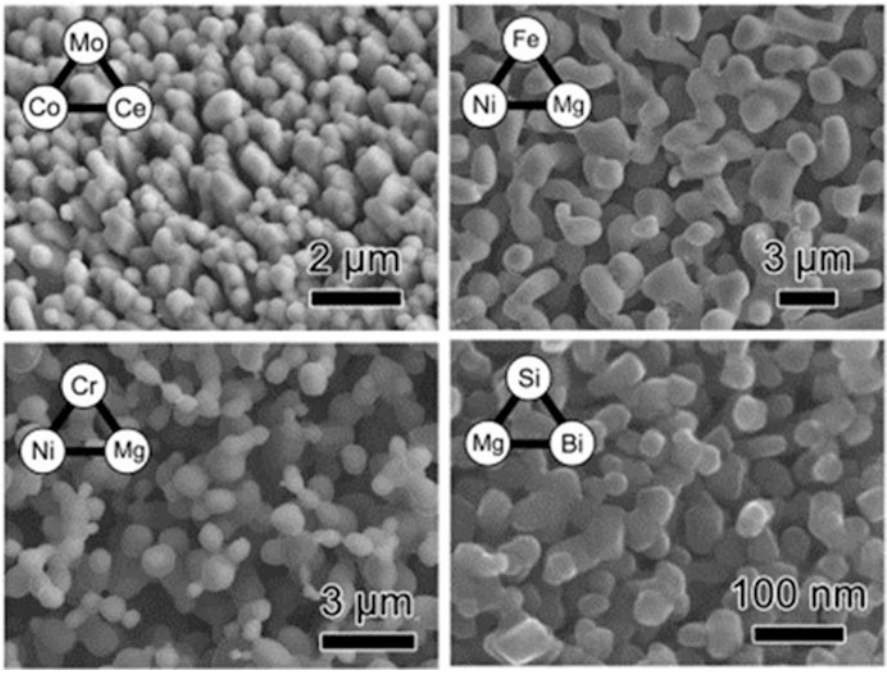

Fig. 8.8 SEM images of the fracture surfaces of porous base metals, Mo, Fe, Cr, and Si together with the corresponding triangle relationship of the enthalpies of mixing used for the preparation

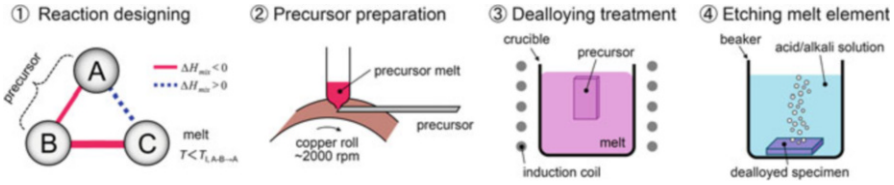

Fig. 8.9 Schematic of the process of porous metal preparation using dealloying within a metallic melt

8.2.2 β-Ti Alloy [9]

In the above section, we outlined the newly proposed concept of dealloying where a metallic melt is used as the dealloying medium. By employing three metal elements that satisfy the triangle relationship of the heats of mixing shown in Fig. 8.2 and also referring to the equilibrium phase diagram database, we confirmed that dealloying actually occurs using a metallic melt, and an open-cell-type nanoporous Ti was successfully prepared, which has never been achieved by conventional dealloying in an aqueous solution. In the next step, we apply our dealloying method for preparing open-cell-type nanoporous metal alloys. To realize this application,

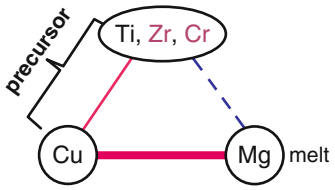

Fig. 8.10 Triangle relationship of the enthalpies of mixing among Ti, Zr, Cr, Cu, and Mg

the triangle relationship is extended wherein the role of element A in Fig. 8.2 is expanded to incorporate additional elements A′, A″, ..., which are similar to element A in terms of their values of heat of mixing with B and C. Based on this strategy, we expect the formation of nanoporous A-A′-A″... alloys under the appropriate dealloying conditions. Here, we demonstrate the preparation of a β-type nanoporous Ti alloy by extending the preparation method for nanoporous Ti described previously. Generally, Ti has a hcp crystal structure at room temperature but has a bcc structure as a high temperature phase. By adding bcc stabilizers, a Ti alloy having a bcc structure, namely, the β-type Ti alloy, can be obtained even at room temperature. Among the potential bcc stabilizers, if those elements which are similar to Ti in terms of its heat of mixing with Cu and Mg are employed as the additional elements in the Ti–Cu precursor, these bcc stabilizers will not dissolve into the Mg melt during dealloying treatment and would thus remain, forming the β-Ti alloy phase with a nanoporous structure. Among these bcc stabilizers, we selected Cr and also Zr as a neutral element for the additional elements because similar to Ti, Cr and Zr can mix with Cu but separate from Mg. These elements satisfy the triangle relationship of the values of heat of mixing shown in Fig. 8.10. A pseudo-binary alloy with a composition of $(Ti_{0.847}Zr_{0.055}Cr_{0.098})_{20}Cu_{80}$ (at%) was employed as the precursor. The dissolving component, Cu, is added to the remaining component, $Ti_{84.7}Zr_{5.5}Cr_{9.8}$ (at%) alloy, which is reported to form the β-Ti alloy at room temperature [22]. Using this precursor, the dealloying reaction in the Mg melt was investigated.

Figure 8.11a (top) shows XRD patterns of the 40 μm thick $(Ti_{0.847}Zr_{0.055}Cr_{0.098})_{20}Cu_{80}$ melt-spun ribbon precursor. The phases present in the as-spun ribbon precursor were a mixture of crystalline Cu and Cu_3Ti. Figure 8.11a (bottom) and 8.11b shows XRD patterns and a back-scattering SEM image from a cross section of the $(Ti_{0.847}Zr_{0.056}Cr_{0.098})_{20}Cu_{80}$ alloy dealloyed in the Mg melt at 973 K for 15 min, respectively. The XRD measurement was performed with the bulk sample prepared under the same conditions as the melt-spun ribbon to enhance the accuracy. These analyses reveal that the precursor composed of Cu and Cu_3Ti phases transformed into a nanocomposite of α-Mg and β-Ti composed of regions about 500 nm in size by dealloying the Cu element in the Mg melt. Figure 8.12 shows (a) bending fracture surface, (b) enlarged surface, (c) EDX spectrum, and (d) TEM image with the electron diffraction pattern in the inset for the porous Ti-based alloy prepared by etching α-Mg from the β-Ti/α-Mg composite using a 3 mol/l nitric acid solution for 30 min followed by washing/drying.

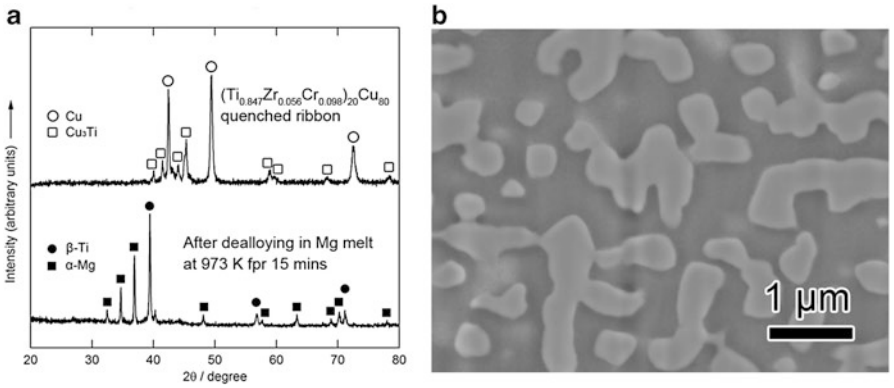

Fig. 8.11 XRD patterns of $(Ti_{0.847}Zr_{0.055}Cr_{0.098})_{20}Cu_{80}$ (at%), as melt spun (*top*) and dealloyed in a Mg melt at 973 K for 15 min (*bottom*) (**a**), and SEM image of the polished surface of the dealloyed sample (**b**) (Reprinted from Ref. [9], Copyright 2011, with permission from Elsevier)

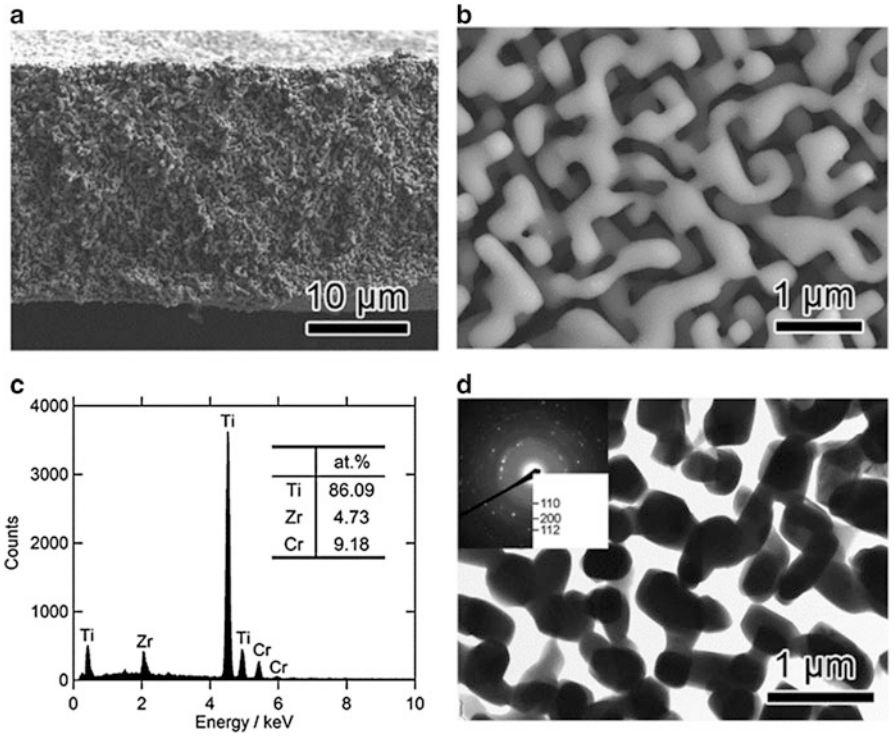

Fig. 8.12 SEM image of the fracture surface of the porous β-Ti alloy (low magnification (**a**) and high magnification (**b**)), EDX spectrum obtained from the surface (**c**), and TEM image of the porous β-Ti alloy together with the electron diffraction pattern in the inset (**d**) (Reprinted from Ref. [9], Copyright 2011, with permission from Elsevier)

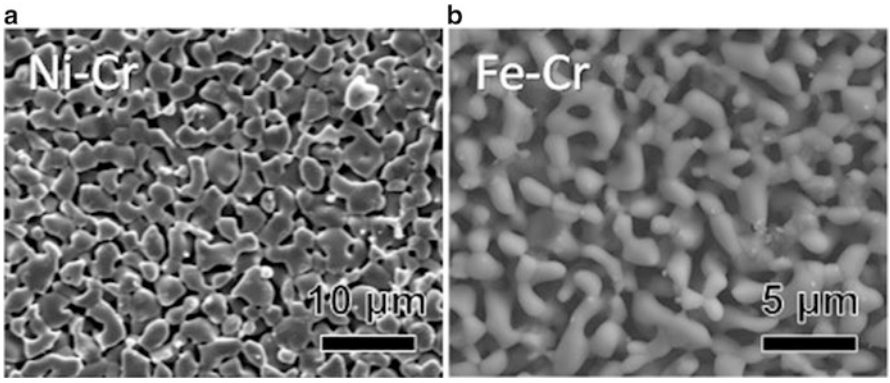

Fig. 8.13 SEM images of the fracture surface of porous Ni–Cr (*left*) and Fe–Cr (*right*) prepared by dealloying within a metallic melt

The SEM image of the cross section (Fig. 8.12a) indicates that the porous structure of a ligament size of about 500 nm is uniformly spread throughout. The corresponding EDX spectrum (Fig. 8.12c) shows that the porous alloy has a composition of $Ti_{86.09}Zr_{4.73}Cr_{9.18}$ (at%), which is nearly the same as that of the initial alloy precursor. No Mg was detected from the fracture surface, indicating that the α-Mg/β-Ti composite alloy had a bicontinuous structure; hence, the resulting nanoporous Ti alloy had an open-cell structure, which is the same as the case of nanoporous α-Ti described previously. These results confirm that the triangle relationship of the heats of mixing shown in Fig. 8.2 can be applied for preparation of nanoporous alloys, as shown in Fig. 8.10. Using this strategy, we have succeeded in preparing open-cell-type nanoporous alloys of base metals such as Ni–Cr alloy [23] and Fe–Cr stainless steel [10], as shown in Fig. 8.13, which have never been prepared by the conventional dealloying method.

8.3 Surface Improvement of Biomedical Ti Alloys by Dealloying with a Metallic Melt

8.3.1 Ni–Ti (Nitinol) [24]

8.3.1.1 Dealloying Treatment in a Metallic Melt

We intend to remove the toxic Ni element from the surface of a Ni–Ti alloy, which has been used for various biomedical applications due to its excellent superelasticity [25]. In order to remove the Ni element from the Ni–Ti alloy by the dealloying reaction, the elements in the triangle relationship given in Fig. 8.2 are designated as A = Ti, B = Ni, and C = Mg, Ca, and RE metals. Here, we selected

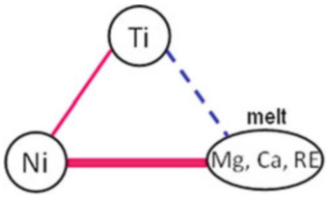

Fig. 8.14 Triangle relationship of enthalpies of mixing among Ti, Ni, and Ce

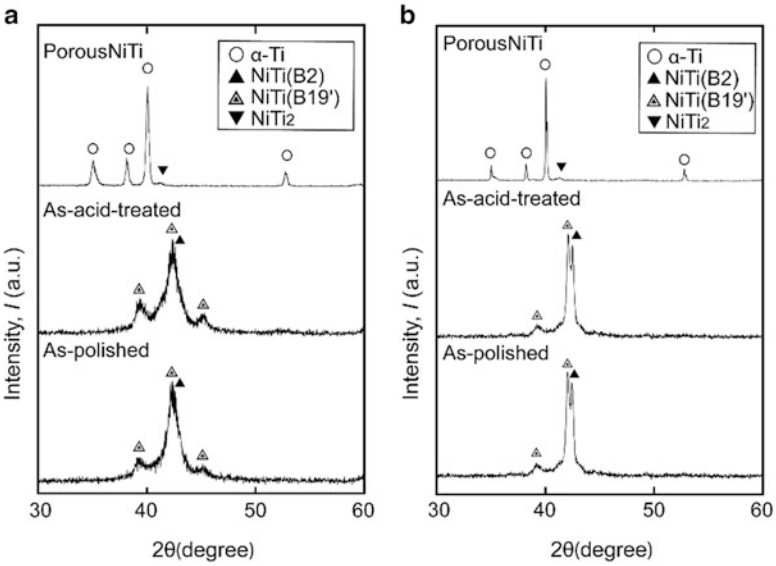

Fig. 8.15 XRD patterns of As-polished, As-acid-treated, and porous NiTi using the α-2θ (**a**) and θ-2θ (**b**) methods (Reprinted from Ref. [24]. Copyright 2010, with permission from Tohoku University, Japan)

Ce (melting point = 1,071 K) as the C element from the potential candidates, which yields the triangle illustrated in Fig. 8.14. The Ce melt bath was prepared in a commercial Ti crucible by the high-frequency induction melting method at 1,073 K under an argon atmosphere. A polished NiTi disk (~1.2 mm in thickness) was tied by a molybdenum wire and then immersed in the Ce melt bath for 0.24 ks to remove the toxic Ni element from the surface. After this dealloying treatment, the disk was immersed in an acid aqueous solution composed of H_2O:HNO_3:HCl = 15:8:3 (vol.) for 2.8 ks at ambient temperature to remove the Ce phases from the surface. After the disk was cleaned by ethanol and ultra-purified water using an ultrasonic cleaner and subsequently dried, the surface modified disks, hereafter referred to as "porous NiTi," were obtained.

Figure 8.15 shows XRD patterns of the surface of the modified disks using the θ-2θ and α-2θ methods for the interior and surface investigations, respectively. The "As-polished" disk, prior to both the dealloying and acid treatments, is found to be

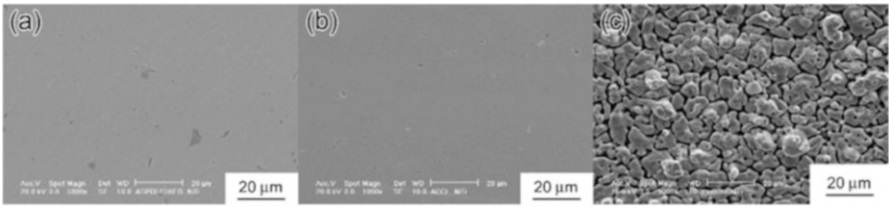

Fig. 8.16 SEM images of the surfaces of As-polished (**a**), As-acid-treated (**b**), and porous NiTi (**c**) (Reprinted from Ref. [24]. Copyright 2010, with permission from Tohoku University, Japan)

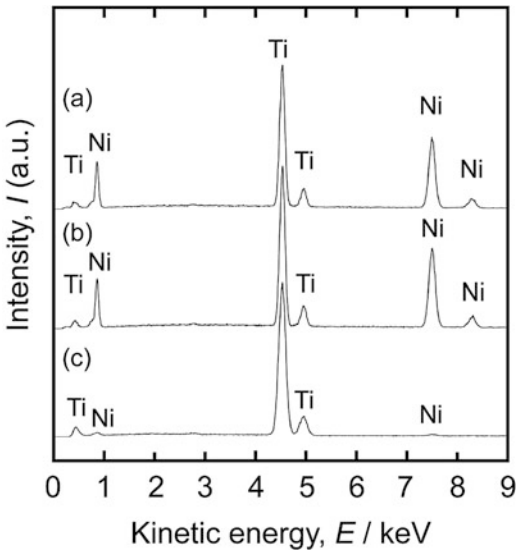

Fig. 8.17 EDX spectra of the surface of (**a**) As-polished, (**b**) As-acid-treated, and (**c**) porous NiTi (Reprinted from Ref. [24]. Copyright 2010, with permission from Tohoku University, Japan)

composed of NiTi with both austenite (B2) and martensite (B19′) phases. The XRD pattern of the α-2θ method exhibits the B19′ peaks more prominently than that of the θ-2θ method. This indicates that the B19′ phase exists around the surface more than the interior; thus, this phase is considered to be generated during the polishing treatment by a stress-induced mechanism. The porous NiTi disk was found to be composed of α-Ti and a $NiTi_2$ intermetallic compound. Figure 8.16 shows surface SEM images of the As-polished (a), As-acid-treated (b), and porous NiTi (c) disks. The porous NiTi disk is thereby confirmed to have a porous surface with a porosity of ~1 μm. From the EDX analysis results shown in Fig. 8.17, the concentration of the Ni element detected from the porous NiTi disk surface clearly decreases due to the dealloying treatment in the Ce melt bath. Table 8.2 shows the concentrations of Ni and Ti in each sample derived from the EDX results. The As-polished sample shows nearly Ni:Ti = 1:1, being the same as the nominal alloy composition. On the other hand, the porous NiTi shows Ni:Ti = 1:9 confirming a decrease in the Ni content. Figure 8.18 shows an SEM image of a cross section of the porous NiTi.

Table 8.2 EDX quantitative analyses of the surface of As-polished, As-acid-treated, and porous NiTi

Specimen	Concentration of elements (at%)		
	Ni	Ti	Total
As-polished	50.67	49.33	100
As-acid-treated	51.71	48.29	100
Porous NiTi	13.47	86.53	100

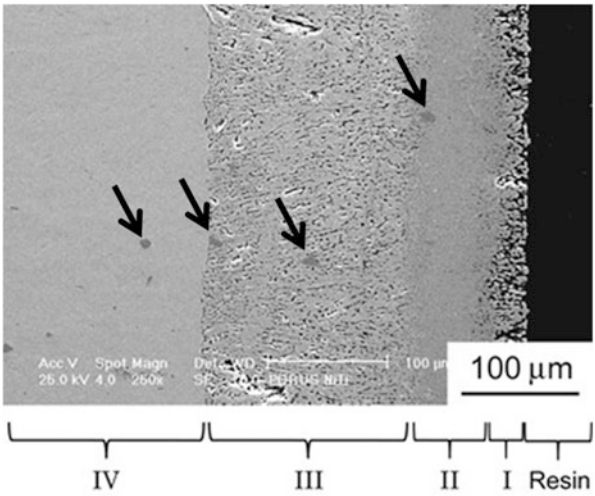

Fig. 8.18 SEM image of a cross section of the porous NiTi. Arrows indicate TiC precipitates (Reprinted from Ref. [24]. Copyright 2010, with permission from Tohoku University, Japan)

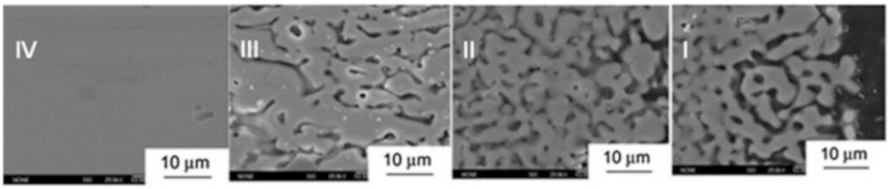

Fig. 8.19 High magnification SEM images of a cross section of the porous NiTi. I~IV correspond to the regions numbered in Fig. 8.18 (Reprinted from Ref. [24]. Copyright 2010, with permission from Tohoku University, Japan)

After the dealloying treatment, a multilayered structure having different porous features is observed at a depth of 200–300 µm. Hereafter, these layers are denoted as Regions I, II, III, and IV, from the outermost surface to the interior, respectively. Enlarged SEM images for each region are shown in Fig. 8.19. Region I exhibits a porous structure and its thickness is about 20 µm. Regions II and III also have a porous structure, but Region II has finer pores than Region III. The thickness of Regions II and III is 60 and 120 µm, respectively. Region IV represents the substrate. TiC precipitates of about 10 µm diameter, appearing as dark-gray regions in Fig. 8.18, originated from the NiTi substrate and can be observed in Regions II

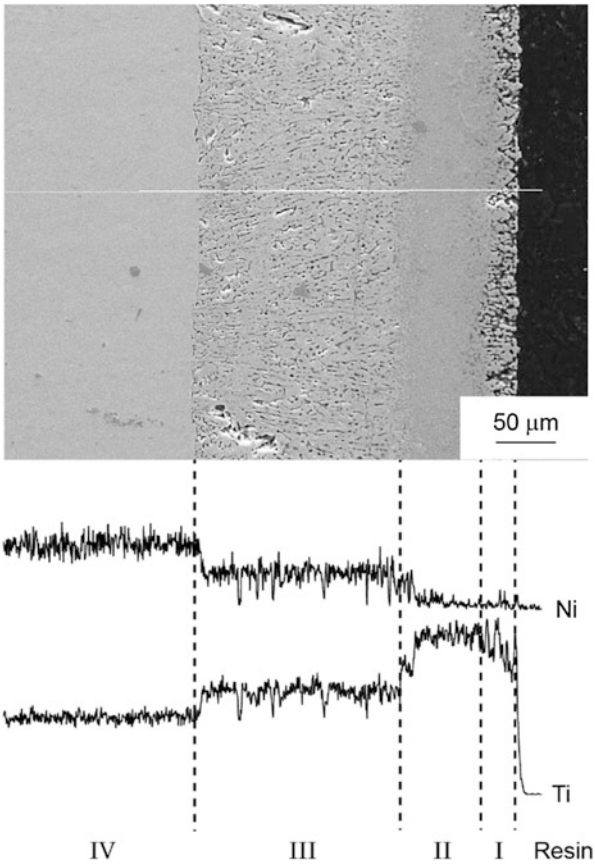

Fig. 8.20 Line analysis of a cross section of the porous NiTi sample. I~IV correspond to the regions numbered in Fig. 8.18 (Reprinted from Ref. [24]. Copyright 2010, with permission from Tohoku University, Japan)

and III, suggesting that the substrate material remained in these regions due to incomplete dealloying treatment. Figure 8.20 shows an EDX composition profile from a line analysis passing from Region IV to Region I in the porous NiTi. The concentration of Ni was found to decrease stepwise while the Ti concentration increased. The Ni concentration in Regions I and II is nearly zero and is about 30 % in Region III. These results indicate that dealloying of Ni occurred from Region I to III to a 200 μm depth. A preliminary experiment using a 40 μm thick NiTi ribbon with a Ce melt revealed that the time required to completely remove Ni from the allow sample using the dealloying method was 0.24 ks; thus, the dealloying rate is estimated to be $\sim 8.3 \times 10^{-2}$ μm/s. Therefore, from these preliminary results, we would expect dealloying to form a porous layer about 20 μm thick on the disk sample. However, in fact, after dealloying, the multilayer structure composed of different porous features was formed to a 200 μm depth. Figure 8.21 shows XRD patterns measured from the porous NiTi after mechanically polishing the surface down to several depths. Each position of the XRD pattern on the left-hand side corresponds to the depth from the surface on the right-hand side SEM image. From

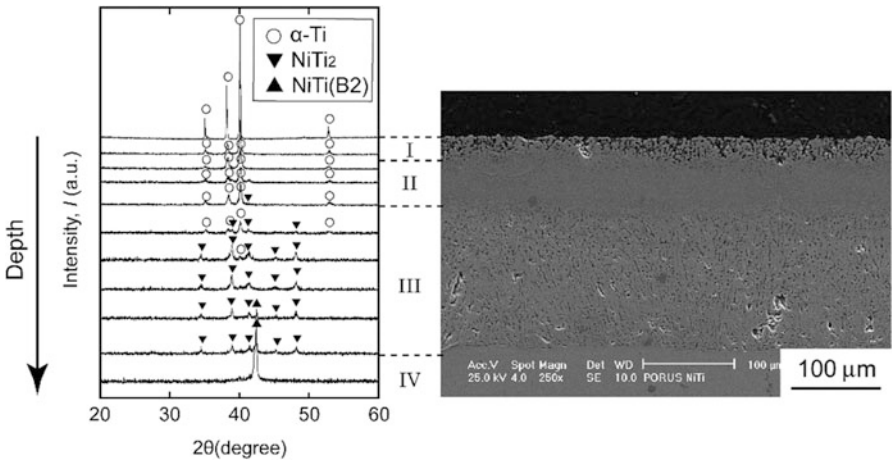

Fig. 8.21 θ-2θ XRD depth profile of the surface of the porous NiTi. I~IV correspond to the regions numbered in Fig. 8.18 (Reprinted from Ref. [24]. Copyright 2010, with permission from Tohoku University, Japan)

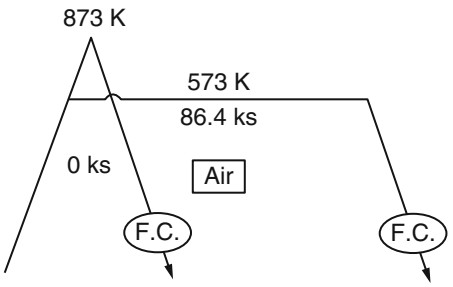

Fig. 8.22 Schematic of the temperature schedule for the oxidization treatment process in air (Reprinted from Ref. [24]. Copyright 2010, with permission from Tohoku University, Japan)

the XRD analysis, Regions I and II were identified as α-Ti phase. Region III was identified as $NiTi_2$ phase. Region IV was identified as an austenite phase, confirming this region as the original NiTi substrate layer.

8.3.1.2 Oxidization Treatment in Air

Surface oxidation of Ti alloy is known for effective way to suppress metal ion release in the simulated body fluid [5, 6]. So in this study, we oxidized surface of the dealloyed porous NiTi alloy for further suppression of Ni ion release and investigated the synergetic effect of dealloying and oxidation on Ni ion release. Oxidization treatment was performed in air using an electric furnace. Figure 8.22 shows the heating program utilized for the oxidization treatment. The As-polished, As-acid-treated, and porous NiTi samples were used. Prior to the oxidization treatment, the samples were washed under ultrasonic vibration in ultra-purified

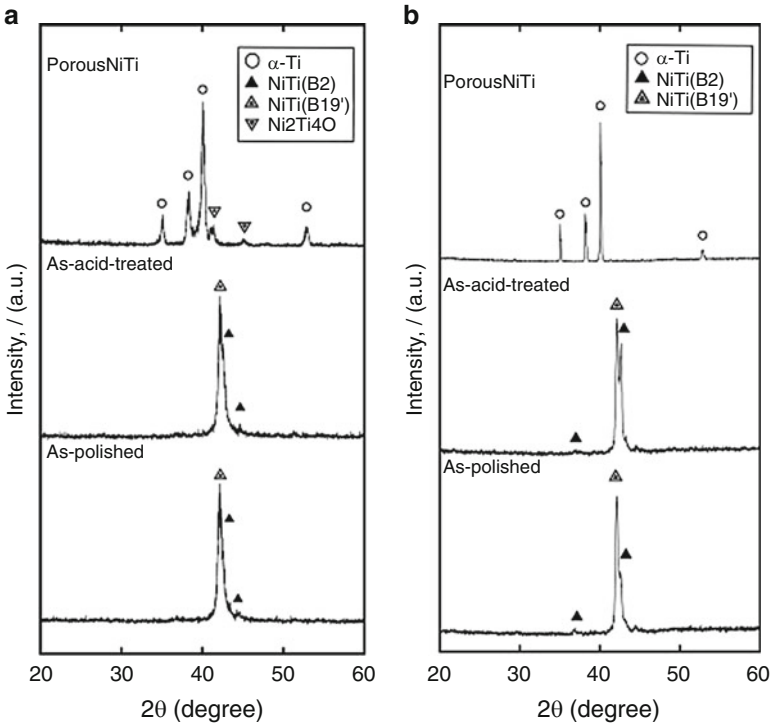

Fig. 8.23 (**a**) α-2θ and (**b**) θ-2θ XRD patterns of As-polished, As-acid-treated, and porous NiTi oxidized in air at 573 K for 86.4 ks (Reprinted from Ref. [24]. Copyright 2010, with permission from Tohoku University, Japan)

water and ethanol for 0.3 ks followed by drying. The holding times were 86.4 ks at 573 K and 0 ks at 873 K (here, "0 ks" means that after reaching 873 K, furnace cooling (FC) began immediately).

8.3.1.3 Phase and Morphology

Figures 8.23 and 8.24 show XRD patterns of the samples oxidized at 573 K for 86.4 ks and 873 K for 0 ks, respectively, under the α-2θ and θ-2θ scanning modes. The titanium oxide phase was not detected from either of the samples oxidized at 573 K for 86.4 ks in air. In the porous NiTi, the Ni_2Ti_4O phase was likely detected. However, because the crystal structure of the Ni_2Ti_4O phase is quite similar to the $NiTi_2$ phase, it was difficult to identify the phase after oxidation treatment by the XRD method. There are some reports of a Ni_2Ti_4O phase forming via the interaction with the oxygen in air [26, 27]. Therefore, we consider that the Ni_2Ti_4O phase formed in the porous NiTi. More detailed investigation is necessary for precise phase identification. Meanwhile, the rutile and Ni_3Ti phases were detected in the

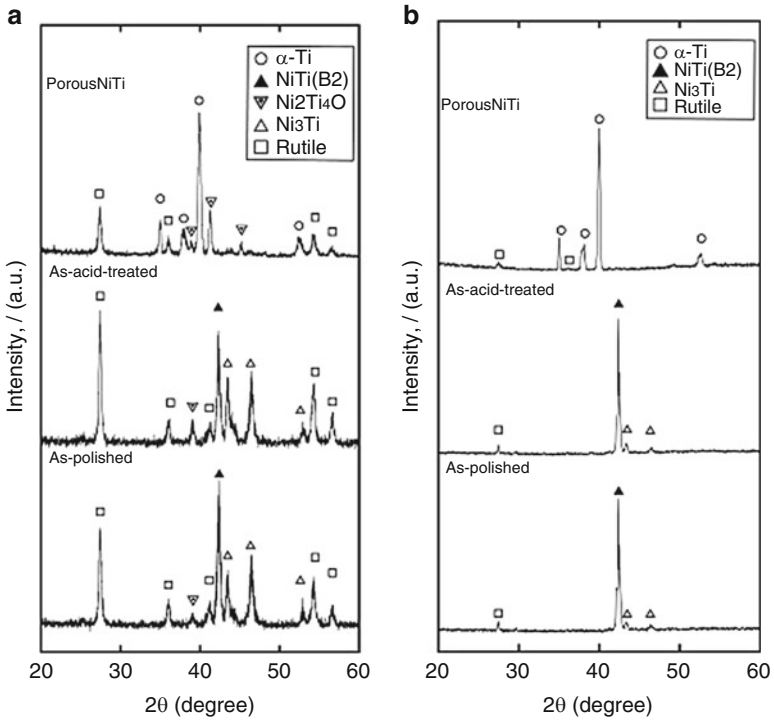

Fig. 8.24 (**a**) α-2θ and (**b**) θ-2θ XRD patterns of As-polished, As-acid-treated, and porous NiTi oxidized in air at 873 K for 0 ks (Reprinted from Ref. [24]. Copyright 2010, with permission from Tohoku University, Japan)

As-polished sample oxidized at 873 K for 0 ks in air. The formation mechanism of the Ni_3Ti phase is considered to be the result of Ti diffusion into the surface oxide layer, wherein the Ti-poor region that formed beneath the oxide layer transformed into a relatively Ni-rich phase, Ni_3Ti. In the porous NiTi, rutile and Ni_2Ti_4O phases were detected. Figures 8.25 and 8.26 show SEM images of the surface features of the samples after oxidation at 573 K for 86.4 ks and 873 K for 0 ks in air, respectively. No obvious change of surface features was observed in the As-polished and As-acid-treated samples before/after oxidation at 573 K for 86.4 ks in air. However, by oxidation at the highest temperature of 873 K for 0 ks in air, oxide particles formed. In the porous NiTi sample, a more strongly interconnected porous structure formed after the oxidation treatment and was more significant for the sample oxidized at 873 K for 0 ks in air. Figure 8.27 shows SEM images of the cross section of the porous NiTi oxidized at the lowest temperature of 573 K for 86.4 ks in air. No obvious change was detected compared to the untreated sample (see Fig. 8.19). Figure 8.28 shows SEM images of the cross section of the porous NiTi oxidized at 873 K for 0 ks in air. After the treatment, the pores in Region II become more significant, and the interface between Regions II and III becomes unclear.

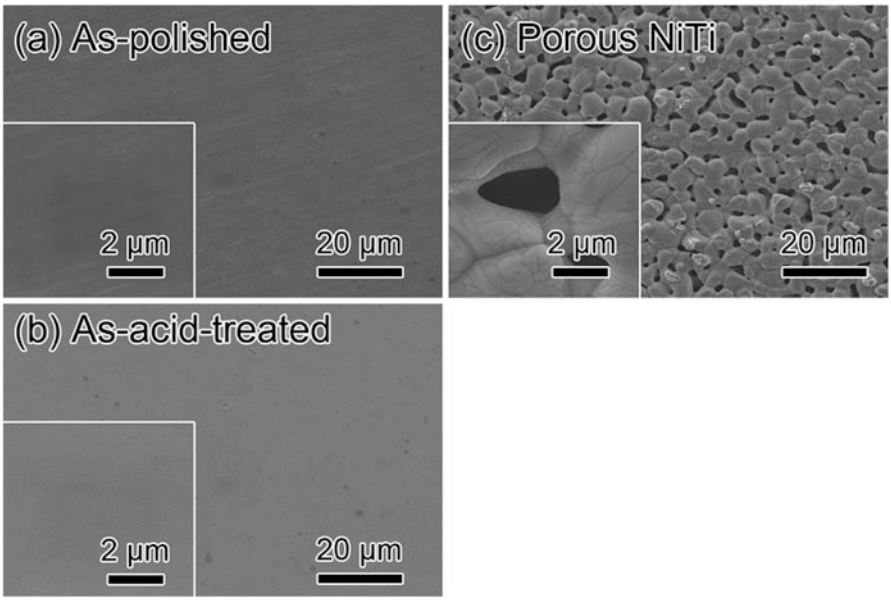

Fig. 8.25 SEM images of the surface of As-polished (**a**), As-acid-treated (**b**), and porous NiTi (**c**) oxidized in air at 573 K for 86.4 ks (Reprinted from ref. [24]. Copyright 2010, with permission from Tohoku University, Japan)

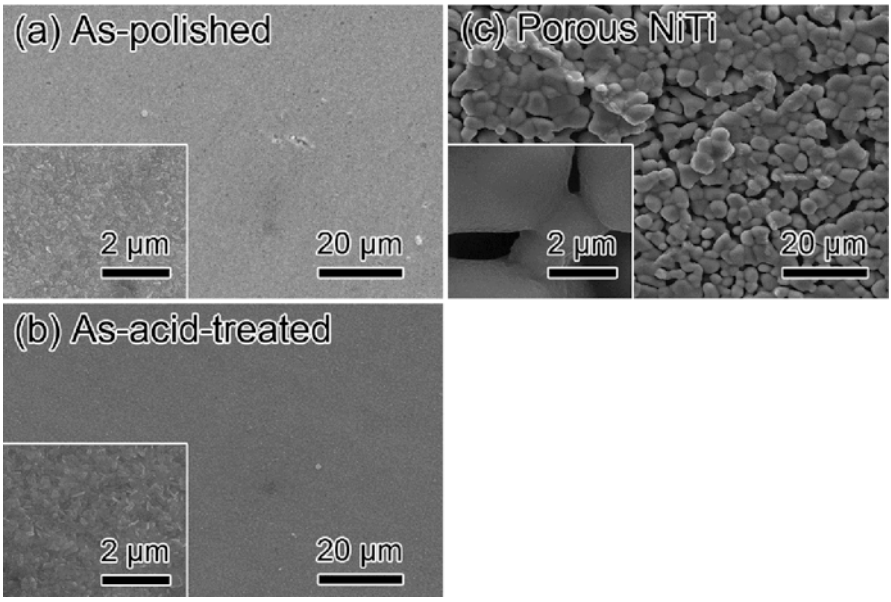

Fig. 8.26 SEM images of the surface of As-polished (**a**), As-acid-treated (**b**), and porous NiTi (**c**) oxidized in air at 873 K for 0 ks (Reprinted from Ref. [24]. Copyright 2010, with permission from Tohoku University, Japan)

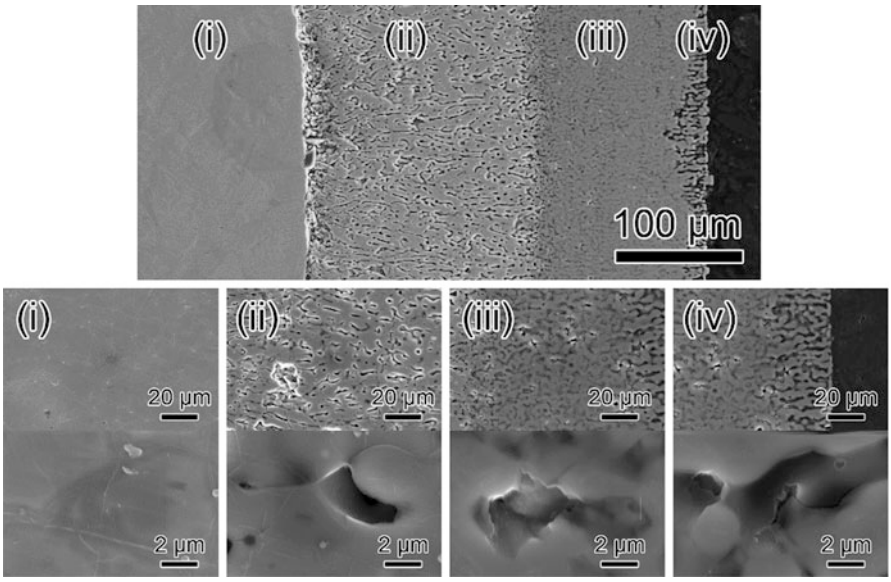

Fig. 8.27 Cross sections of porous NiTi oxidized in air at 573 K for 86.4 ks (Reprinted from ref. [24]. Copyright 2010, with permission from Tohoku University, Japan)

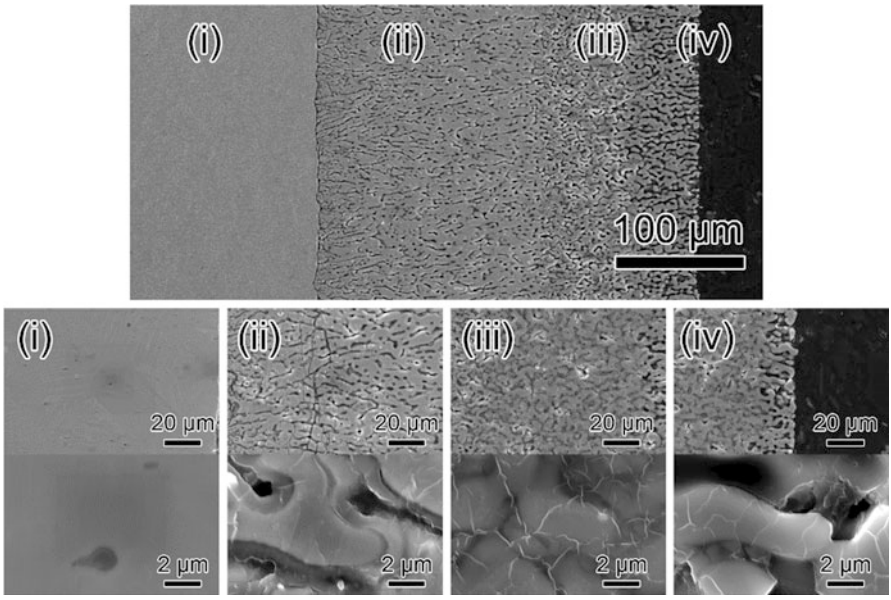

Fig. 8.28 Cross sections of porous NiTi oxidized in air at 873 K for 0 ks (Reprinted from Ref. [24]. Copyright 2010, with permission from Tohoku University, Japan)

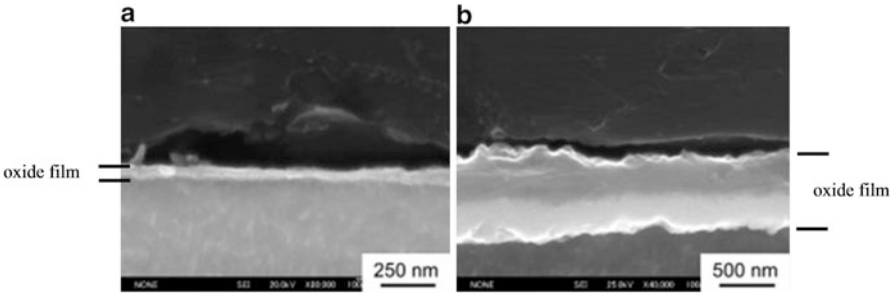

Fig. 8.29 Cross section of As-polished oxidized in air (**a**) at 573 K for 86.4 ks and (**b**) at 873 K for 0 ks (Reprinted from Ref. [24]. Copyright 2010, with permission from Tohoku University, Japan)

8.3.1.4 Thickness and Composition Profile

Figure 8.29 shows SEM images of the surface region of the cross section of the As-polished sample after oxidation treatment. For oxidization at 573 K for 86.4 ks in air, an oxide film of about 50 nm thickness was formed, which is thinner than the detection limit of the XRD technique. Therefore, no obvious diffraction from the oxide film was detected from the XRD pattern even using the α-2θ scanning mode (Fig. 8.23a). The thickness of the oxide film formed by oxidation at 873 K for 0 ks in air was about 500–700 nm. The As-acid-treated sample exhibits a similar XRD pattern (Fig. 8.24a), indicating that the thickness of the oxide film is very similar to that of the As-polished sample. In the porous NiTi sample, the cross section could not be observed because the mechanical polishing damaged the fragile surface of the porous structure. However, the surface oxide film that formed at the lower oxidation temperature was considered to be thin. Hence, the surface oxide film that developed at 573 K is expected to have good adhesion to the substrate. For microstructural observation of the oxidized porous NiTi sample, the focused ion beam (FIB) technique is useful for fabricating cross sections. Figure 8.30 shows a line analysis of the EDX composition profile of the porous NiTi sample oxidized under various conditions in air from the sample center to the surface. In the sample oxidized at 573 K for 86.4 ks in air, oxygen was detected from Region I to Region III, and its intensity is stronger in Region III, suggesting that oxidation proceeded to this depth. Similarly, in the porous NiTi sample oxidized at 873 K for 0 ks in air, oxygen was detected from Region I to Region III.

8.3.1.5 Evaluation of Ni and Ti Ion Release Behavior in Simulated Body Fluid

Figure 8.31 shows the immersion time dependence of Ni and Ti ion release from the porous NiTi sample in a 1 mass% lactic acid solution after 86.4 ks (1 day), 259.2 ks (3 days), and 604.8 ks (7 days). The Ni and Ti ion release increase with increasing immersion time. Figure 8.32 shows the immersion time dependence of Ni and Ti

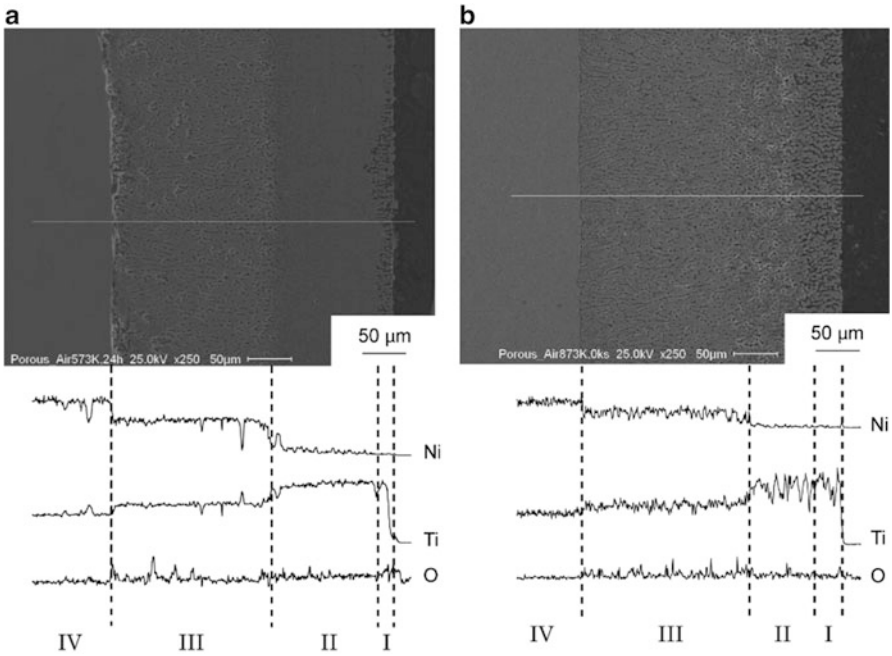

Fig. 8.30 Line analyses of cross sections of porous NiTi oxidized in air at 573 K for 86.4 ks (**a**) and at 873 K for 0 ks (**b**) (Reprinted from Ref. [24]. Copyright 2010, with permission from Tohoku University, Japan)

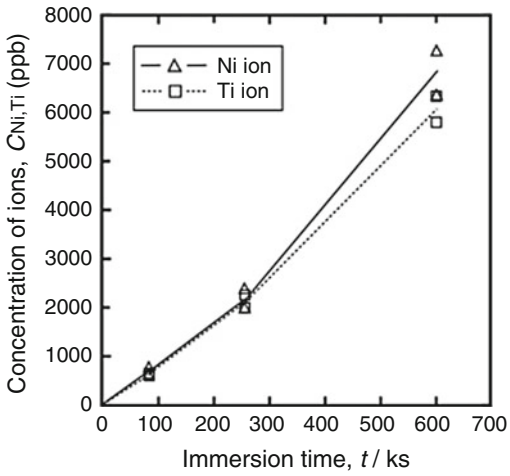

Fig. 8.31 Concentration of released Ni and Ti ions from porous NiTi into a 1 mass% lactic acid solution after 86.4 ks (1 day), 259.2 ks (3 days), and 604.8 ks (7 days) (Reprinted from ref. [24]. Copyright 2010, with permission from Tohoku University, Japan)

ion release from the As-polished and As-acid-treated samples in a 1 mass% lactic acid solution after 1, 3, and 7 days. For the As-polished sample, the Ni ion release decreases with increasing immersion time, while that of the Ti ion increases linearly

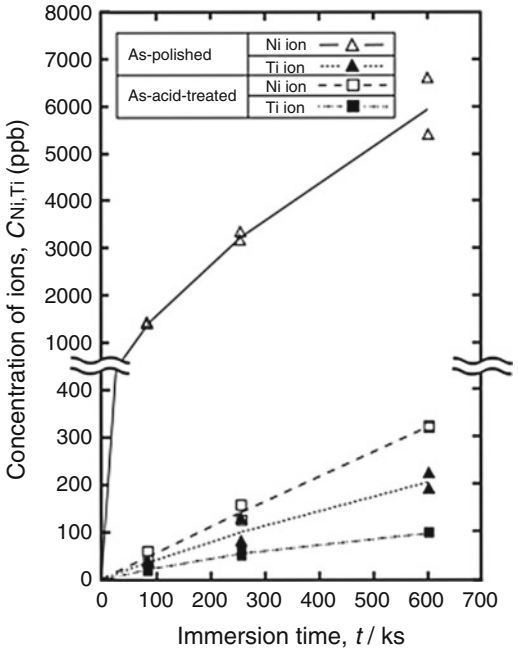

Fig. 8.32 Concentration of released Ni and Ti ions from As-polished and As-acid-treated NiTi into a 1 mass% lactic acid solution after 86.4 ks (1 day), 259.2 ks (3 days), and 604.8 ks (7 days) (Reprinted from Ref. [24]. Copyright 2010, with permission from Tohoku University, Japan)

with increasing immersion time. Figure 8.33 shows a comparison of Ni and Ti ion release among all samples in a 1 mass% lactic acid solution after 7 days. The table at the bottom of the figure summarizes the conditions of sample preparation and concentrations of ion release. Concentrations of released Ni and Ti ions are 6,010 ppb and 208 ppb, respectively, from the As-polished and 6,930 ppb and 6,059 ppb, respectively, from the porous NiTi sample. There was no significant difference in the concentration of Ni ion release between these samples. Considering that the porous NiTi sample has a much larger surface area than that of the As-polished sample, it can be concluded that the dealloying treatment in the Ce melt performs well for reducing the extent of Ni ion release. The As-polished sample oxidized at 573 K for 86.4 ks in air showed Ni and Ti ion release concentrations of 3,167 ppb and 69 ppb, respectively, being lower than those of the As-polished sample. On the other hand, the As-polished sample oxidized at 873 K for 0 ks in air shows Ni and Ti ion release concentrations of 8,034 ppb and 343 ppb, respectively, being larger than those of the As-polished sample. The porous NiTi samples oxidized under both conditions resulted in a diminished Ni ion release, and especially, the oxidization treatment at 537 K for 86.4 ks in air was found to be the most effective for reducing Ni ion release, which is the same tendency demonstrated by the As-polished samples. A depth profile by XRD of the porous NiTi suggests that the 1 mass% lactic acid solution penetrated into Region III containing the $NiTi_2$ phase and contacted with Region IV (the substrate). These regions, which are more enriched by Ni, thus released more Ni ions. As a result, the porous NiTi sample released a higher concentration of Ni ions than the As-polished sample. The

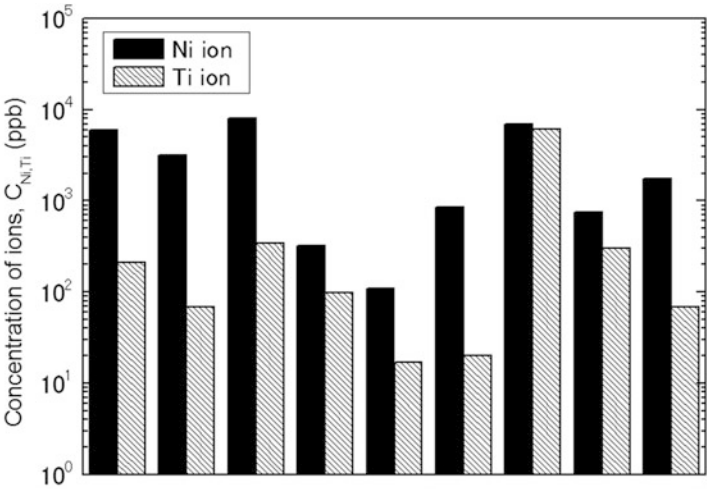

Polish		○	○	○	○	○	○	○	○	○
Immersion	Molten Ce	×	×	×	×	×	×	○	○	○
	Acid solution	×	×	×	○	○	○	○	○	○
Gas oxidation	573 K, 86.4 ks	×	○	×	×	○	×	×	○	×
	873 K, 0 ks	×	×	○	×	×	○	×	×	○
Concentration of ions (ppb)	Ni ion	6010	3167	8034	322	109	843	6930	758	1756
	Ti ion	208	69	343	98	17	20	6059	305	68

Fig. 8.33 Concentration of released Ni and Ti ions from each specimen treated under various conditions into a 1 mass% lactic acid solution after 604.8 ks (7 days) immersion (Reprinted from Ref. [24]. Copyright 2010, with permission from Tohoku University, Japan)

increased Ti ion release from the porous NiTi sample was caused mainly by the greatly increased surface area. The specific surface area of the porous NiTi can be roughly estimated to be the range of 1~10 m^2/g, based upon another dealloying study for porous Nb [11]. By adopting this result, the surface area of the porous NiTi (~0.3 g) was estimated to be 0.3~3 m^2, which is ~$10^{4\sim5}$ times larger than that of the As-polished sample (1.25×10^{-4} m^2). Although the increase of surface area caused by the dealloying treatment is very large, the increase of Ni ion release is not so high, indicating that Ni ion release from a unit surface area efficiently decreased. However, when we compare the Ni ion release from samples with the same dimensions, the total amount of Ni ion release is more important than that from the unit surface area. Further optimization on the dealloying conditions for suppressing an increase in the surface area by the dealloying treatment is required to reduce the absolute value of the Ni ion release.

8.3.1.6 Effect of Oxidization on the Ion Release

Oxidation treatment on the As-polished sample at 537 K for 86.4 ks in air resulted in decreased ion release. However, the oxidization treatment at 873 K for 0 ks in air resulted in an increased Ni ion release. Firstov has reported that oxidization treatments at 537–773 K in air formed flat oxide films, while those at 837–1,073 K formed roughened and nanoporous oxide films [28]. Sugawara et al. reported the formation of an amorphous Ti oxide film on the NiTi alloy by oxidization treatment below 773 K in a gas mixture consisting of 80 % N_2 and 20 % O_2 [29]. This suggests that the reduced Ni ion release from the sample oxidized at 573 K for 86.4 ks in air was caused by the formation of a dense amorphous oxide layer by oxidation treatment, which in the present study effectively acted as a barrier against Ni ion release. By the oxidization treatment at 873 K for 0 ks in air, the formation of oxide particles on the titanium oxide surface is observed, as described in the Section of 8.3.1.3, which is in agreement with the phenomena reported by Firstov and Sugawara. Due to roughening of the surface film by oxidation at 873 K for 0 ks in air, a pathway for Ni ion release was formed in the titanium oxide film, resulting in a reduced barrier effect against Ni ion release. In addition, as shown in Fig. 8.23, formation of Ni_3Ti phase on the surface was observed, which also contributed to a greater Ni ion release from the sample.

8.4 Summary

Using the dealloying method in a metallic melt, selective removal of toxic Ni element from the surface of NiTi alloy, which has been used as a biomedical metal, was attempted in order to improve their biocompatibility.

1. By immersing NiTi into a Ce melt, the Ni concentration on the surface of the NiTi alloy was drastically reduced while developing a porous Ti surface layer.
2. Although a drastic decrease of surface Ni concentration was demonstrated, Ni ion release from the dealloyed NiTi in a lactic acid aqueous solution was found to slightly decrease from that of nontreated NiTi. This is considered to be due to the substantially increased surface area, which is ~$10^{4\sim5}$ times larger than that of the original sample, induced by the dealloying treatment, although Ni ion release per unit of surface area of the dealloyed sample was successfully decreased.
3. By surface oxidation treatment of the dealloyed NiTi at 537 K in air, ion release in the lactic acid aqueous solution was found to be suppressed.

More research is required to optimize the dealloying conditions that can realize a reduction of the surface concentration of a toxic element without increasing the surface area. Additionally, more effective surface treatments can be achieved by applying the dealloying method together with a carefully crafted subsequent surface oxidation treatment.

References

1. Wu SK, Lin HC, Lee CY (1999) Gas nitriding of an equiatomic TiNi shape memory alloy. II. Surf Coat Technol 113:13–16
2. Lahann J, Klee D, Pluester W, Hoecker H (2001) Bioactive immobilization of r-hirudin on CVD-coated metallic implant devices. Biomaterials 22:817–826
3. Poon RWY, Yeung KWK, Liu XY, Chu PK, Chung CY, Lu WW (2005) Carbon plasma immersion ion implantation of nickel-titanium shape memory alloys. Biomaterials 26:2265–2272
4. Zhao XK, Cai W, Zhao LC (2002) Corrosion behavior of phosphorus ion-implanted Ni50.6Ti29.4 shape memory alloy. Surf Coat Technol 155:236–238
5. Liu JX, Yang DZ, Shi F, Cai YJ (2003) Sol-gel deposited TiO_2 film on NiTi surgical alloy for biocompatibility. Thin Solid Films 429:225–230
6. Chu CL, Chung CY, Chu PK (2006) Surface oxidation of NiTi shape memory alloy in a boiling aqueous solution containing hydrogen peroxide. Mater Sci Eng A 417:104–109
7. Man HC, Cui ZD, Yue TM (2001) Corrosion properties of laser surface melted NiTi shape memory alloy. Scr Mater 45:1447–1453
8. Wada T, Yubuta K, Inoue A, Kato H (2011) Dealloying by metallic melt. Mater Lett 65:1076–1078
9. Wada T, Setyawan AD, Yubuta K, Kato H (2011) Nano- to submicro-porous beta-Ti alloy prepared from dealloying in a metallic melt. Scr Mater 65:532–535
10. Wada T, Kato H (2013) Three-dimensional open-cell macroporous iron, chromium and ferritic stainless steel. Scr Mater 68:723–726
11. Kim JW, Wada T, Kim SG, Kato H (2014) Sub-micron porous niobium solid electrolytic capacitor prepared by dealloying in a metallic melt. Mater Lett 116:223–226
12. Tsuda M, Wada T, Kato H (2013) Kinetics of formation and coarsening of nanoporous α-titanium dealloyed with Mg melt. J Appl Phys 114(1–8):113503
13. Raney M (1925) Method of preparing catalytic material. US patent 1,563,587, 1 Dec 1925
14. Khaidar M, Allibert C, Driole GP (1982) Composition, structure and crystallite size of Raney catalysts proceeding from several Ni-Al and Fe-Al intermetallic phases. Mater Res Bull 17:329–337
15. Hotta K, Kuromatsu T (1972) Kinetics of liquid-phase hydrogenation of aliphatic α, β-unsaturated aldehyde over Raney cobalt catalyst modified with Co-, Mn-, Ni-, and $PdCl_2$. Bull Chem Soc Jpn 45:3118–3121
16. Forty AJ (1979) Corrosion micromorphology of noble metal alloys and depletion gilding. Nature 282:597–598
17. Erlebacher J, Seshadri R (2009) Hard materials with tunable porosity. MRS Bull 34:561–568
18. Boer FR, Perrifor DG (1988) Cohesion in metals. Elsevier Science Publishers B.V, Amsterdam
19. Takeuchi A, Inoue A (2005) Classification of bulk metallic glasses by atomic size difference, heat of mixing and period of constituent elements and its application to characterization of the main alloying element. Mater Trans 46:2817–2829
20. ASM Alloy Phase Diagram Database (2014) ASM international, Materials Park. http://www1.asminternational.org/AsmEnterprise/APD. Accessed 25 Feb 2014
21. Wada T, Yubuta K, Ichitsubo T, Segawa H, Yoshida H, Kato H (2014) Three-dimensional nanoporous silicon for lithium ion rechargeable battery negative electrode by dealloying with metallic melt (unpublished research)
22. Cheng CH, Hsu HC, Wu SC, Wang HW, Ho WF (2009) Effects of chromium addition on structure and mechanical properties of Ti-10Zr alloy. J Alloys Compd 484:524–528
23. Suzuki T, Tsuda M, Setyawan AD, Wada T, Kato H (2014) (unpublished research)
24. Hirohashi M (2010) Surface modification of NiTi for biomedical applications. Bachelor thesis, Tohoku University Japan
25. Hornbogen E (1999) Ausforming of NiTi. J Mater Sci 34:599–606

26. Chuprima VG, Shalya IM (2002) Reaction of TiNi with oxygen. Powder Metall Met Ceram 41:85–89
27. Khodorenko VN, Soldatova MI, Gyunter VE (2011) Effect of the composition of a titanium nickelide alloy on its structure and on the formation of the grain boundary ensemble. Russ Phys J 53:827–834
28. Firstov GS, Vitchev RG, Kumar H, Blanpain B, Van Humbeeck J (2002) Surface oxidation of NiTi shape memory alloy. Biomaterials 23:4863–4871
29. Sugawara H, Goto H, Komotori J (2006) Effect of thermal oxidation treatment on surface characteristic and corrosion resistance of NiTi shape memory alloy. J Soc Mater Sci Jpn 55:965–970